High precision ^{89}Y(α,α)^{89}Y scattering at low energies

G. G. Kiss,[1,*] P. Mohr,[2] Zs. Fülöp,[1] D. Galaviz,[3,†] Gy. Gyürky,[1] Z. Elekes,[1] E. Somorjai,[1] A. Kretschmer,[4] K. Sonnabend,[4] A. Zilges,[5] and M. Avrigeanu[6]

[1]*Institute of Nuclear Research (ATOMKI), H-4001 Debrecen, Hungary*
[2]*Diakonie-Klinikum, D-74523 Schwäbisch Hall, Germany*
[3]*Instituto de Estructura de la Materia, CSIC, E-28006 Madrid, Spain*
[4]*Institut für Kernphysik, Technische Universität Darmstadt, D-64289 Darmstadt, Germany*
[5]*Institut für Kernphysik, Universität zu Köln, D-50937 Köln, Germany*
[6]*Horia Hulubei National Institute for Physics and Nuclear Engineering, RO-76900 Bucharest, Romania*

(Received 18 August 2009; published 23 October 2009)

Elastic scattering cross sections of the ^{89}Y(α,α)^{89}Y reaction have been measured at energies $E_{\mathrm{c.m.}} = 15.51$ and 18.63 MeV. The high-precision data for the semimagic $N = 50$ nucleus ^{89}Y are used to derive a local potential and to evaluate the predictions of global and regional α-nucleus potentials. The variation of the elastic α-scattering cross sections along the $N = 50$ isotonic chain is investigated by a study of the ratios of angular distributions for ^{89}Y(α,α)^{89}Y and ^{92}Mo(α,α)^{92}Mo at $E_{\mathrm{c.m.}} \approx 15.51$ and 18.63 MeV. This ratio is a very sensitive probe at energies close to the Coulomb barrier, where scattering data alone is usually not enough to characterize the different potentials. Furthermore, α-cluster states in $^{93}\mathrm{Nb} = {}^{89}\mathrm{Y} \otimes \alpha$ are investigated.

DOI: 10.1103/PhysRevC.80.045807 PACS number(s): 24.10.Ht, 25.55.Ci, 26.30.−k

I. INTRODUCTION

α-nucleus potentials are basic ingredients for the calculation of reaction cross sections with α particles in the entrance or exit channel. These reaction cross sections are included in the calculation of stellar reaction rates in nuclear astrophysics that have to be determined at stellar temperatures corresponding typically to sub-Coulomb energies for reactions involving α particles.

In several astrophysical applications—such as modeling the nucleosynthesis in explosive scenarios like the p process—the reaction rates are taken from statistical model calculations [1,2]. These calculations utilize global α-nucleus optical potential parameter sets. Considerable efforts have been devoted in recent years to improving the knowledge of the α-nucleus optical potential [3–6]. The extensive use of the statistical model calculations requires further experimental tests for the global parametrizations.

The optical potential combines a Coulomb term with a complex nuclear potential, composed of real and imaginary parts. The variation of the potential parameters of the real part as a function of mass and energy is smooth and relatively well understood [7]. On the contrary, the imaginary part of the optical potential is strongly energy-dependent especially at energies around the Coulomb barrier. Therefore, tests of global α-nucleus potentials need to focus on experimental information at energies as close as possible to the astrophysically relevant energy region. One possible way of testing the different potential parametrizations is to carry out α elastic-scattering experiments and compare the measured angular distributions to the corresponding predictions from the global potential parametrizations. However, at astrophysical energies the α-nucleus elastic-scattering cross section is nondiffractive and dominated by the Rutherford component. Therefore, the experiments have to be carried out at slightly higher energies with high precision. From the analysis of the measured angular distributions the parameters of the potential can be derived and have to be extrapolated down to the astrophysically relevant energy region where the relevant α-particle-induced reactions are taking place.

The present study focuses on the determination of optical potentials from elastic-scattering cross sections. It is an interesting and still open question whether reaction cross sections can be predicted from such a potential that has been adjusted only to scattering data. But it remains as a final goal to find a perfect potential that is able to reproduce elastic scattering and reaction cross sections and furthermore properties of cluster states like excitation energies and decay widths.

Several α elastic-scattering experiments on even-even nuclei ^{92}Mo, ^{106}Cd, ^{112,124}Sn, and ^{144}Sm have been performed at ATOMKI in recent years [8–11] to investigate the behavior of α-nucleus optical potentials. This work presents the elastic-scattering experiment performed on the ^{89}Y nucleus to study further the systematic behavior of the optical potentials at low energies. In all of these cases complete angular distributions have been measured at energies close to the Coulomb barrier. The chosen energies were low enough to be close to the region of astrophysical interest and high enough that the scattering cross section differs sufficiently from the Rutherford one.

Previous studies have focused on semimagic even-even nuclei with $N = 82$ (^{144}Sm), $N = 50$ (^{92}Mo), and $Z = 50$ (^{112,124}Sn). As a natural extension of previous work, we are presently working on nuclei that are either nonmagic or even-odd nuclei. Thus, a main motivation for our latest experiment

*ggkiss@atomki.hu; Present address: Laboratori Nazionali del Sud, INFN, Catania, Italia.
†Present address: Centro de Física Nuclear da Universidade de Lisboa, 1649-003, Lisbon, Portugal.

on the nonmagic nucleus ^{106}Cd was to analyze the influence of shell closures on the α-nucleus potential [9]. As a continuation of the systematic study of the behavior of the optical potentials, this work presents the elastic-scattering experiment performed on the neutron-magic ($N = 50$), proton-odd ($Z = 39$) nucleus ^{89}Y. Angular distributions have been measured at $E_{\mathrm{c.m.}} =$ 15.51 and 18.63 MeV, just above the Coulomb barrier (the height of the Coulomb barrier for the $^{89}\mathrm{Y} \otimes \alpha$ system is about 15 MeV). At these energies a reliable test for the global parametrization is possible using the new high-precision data. Furthermore, we can use data from the literature [12,13] to investigate the variation of the imaginary part of the optical potential between $E_{\mathrm{c.m.}} \approx 15.5$ and 23.9 MeV in small steps of approximately 2 MeV. In addition, experimental angular distributions are available at higher energies [14–17]. A local optical potential for ^{89}Y can be established from these data over a wide range of energies. This was a further motivation to study α scattering on ^{89}Y.

A global α-nucleus optical potential must be able to provide a correct prediction for the elastic scattering cross section and to describe the variation of the angular distributions along isotopic and isotonic chains. This is especially important for the extrapolation to unstable nuclei where the potential cannot be derived from experimental scattering data. Galaviz *et al.* [10] measured the elastic-scattering cross sections of the ^{112,124}Sn(α,α)^{112,124}Sn reactions at $E_\alpha = 19.5$ MeV over a broad angular range with small uncertainties of about ≈3–4%. The study of both the proton- and neutron-rich stable tin isotopes provided important information about the changes of the potential parameters with the neutron number along the $Z = 50$ isotopic chain. The ratio of the measured cross sections showed an oscillation pattern that was very pronounced in the backward angle region. The analysis of this ratio provides a further constraint for global α-nucleus potentials, in particular for the extrapolation to unstable nuclei. It must be emphasized that all global α-nucleus optical potentials failed to reproduce either the amplitude or the phase of this oscillation pattern in the ratio of the measured angular distributions of ^{112}Sn and ^{124}Sn at backward angles [10]. This oscillation feature of the experimental data was first observed using our precise data on ^{112}Sn and ^{124}Sn, but it was hidden previously because the typical uncertainties of the elastic-scattering cross sections were of the order of 10–15% [18].

As an extension of our previous work on the isotopic chain at $Z = 50$, now we investigate the behavior of the optical potential parameters along the $N = 50$ isotonic chain. We have measured α scattering data of ^{89}Y with small uncertainties over the whole angular range. This is a prerequisite to study the ratio of the Rutherford normalized cross sections of ^{89}Y(α,α)^{89}Y from this work and ^{92}Mo(α,α)^{92}Mo previously studied by Fülöp *et al.* [8] at $E_{\mathrm{c.m.}} = 13.20, 15.69$, and 18.62 MeV. Further studies could be done on the $N = 50$ nuclei ^{86}Kr, ^{87}Rb, and ^{88}Sr. Low-energy data for the $N = 50$ nucleus ^{90}Zr at 15 MeV [19] were already analyzed in Ref. [7].

This article is organized as follows. In Sec. II we describe our experimental procedure. In a first analysis a local optical potential is derived from the new experimental data and the available scattering data in literature, and furthermore bound-state properties of cluster states in the nucleus $^{93}\mathrm{Nb} = {}^{89}\mathrm{Y} \otimes \alpha$ are studied (Sec. III). The measured angular distributions as well as the ratio of the elastic-scattering cross sections of the two $N = 50$ nuclei ^{89}Y and ^{92}Mo are compared to predictions using several global optical potential parametrizations in Sec. IV; additionally, calculations are compared to angular distributions at higher energies and to excitation functions from literature [12,13]. Finally, conclusions are drawn in Sec. V.

II. EXPERIMENTAL TECHNIQUE

The experiment was carried out at the cyclotron laboratory of ATOMKI, Debrecen. A similar experimental setup was used also in the previous experiments [8–11] and is described in more detail in Ref. [20]. The following paragraphs provide a short description of the experimental procedure.

A. Targets and scattering chamber

The targets were produced by evaporation of metallic yttrium onto thin carbon foils (≈20 μg/cm^2). The target thickness was approximately 200 μg/cm^2. The targets were mounted on a remotely controlled target ladder in the center of the scattering chamber. The stability of the targets was checked continuously with monitor detectors (see below) during the experiment.

The $E_{\mathrm{lab}} = 16.21$ and 19.47 MeV energy α beam (beam current: 150 pnA) was led to the scattering chamber through an analyzing magnet. Because the energy stability of the beam is important for the experiment, the widths of the slits at the entrance and the exit of the magnet were small (1 mm). Moreover, the beam energy was monitored during the experiment with the monitor detectors (see below). The total uncertainty of the beam energy was found to be less than 0.5%.

An aperture of 2 × 6 mm was mounted on the target ladder to check the beam position and size of the beamspot before and after every change of the beam energy or current. We optimized the beam until not more than 1% of the total beam current could be measured on this aperture. As a result of the procedure, the horizontal size of the beamspot was below 2 mm during the whole experiment, which is crucial for the precise determination of the scattering angle.

B. Detectors and data acquisition

Four ion implanted silicon detectors with active areas of 50 mm^2 were used for the measurement of the angular distributions. The detectors were mounted in pairs separated by 10°. The solid angles covered by the two detector pairs were $\Delta\Omega = 1.56 \times 10^{-4}$ and $\Delta\Omega = 1.81 \times 10^{-4}$. The ratios of solid angles of the different detectors were checked by measurements at overlapping angles with good statistics.

In addition, two detectors were mounted at a larger distance on the wall of the scattering chamber at fixed angles $\vartheta = \pm 15°$ left and right to the beam axis. These detectors were used

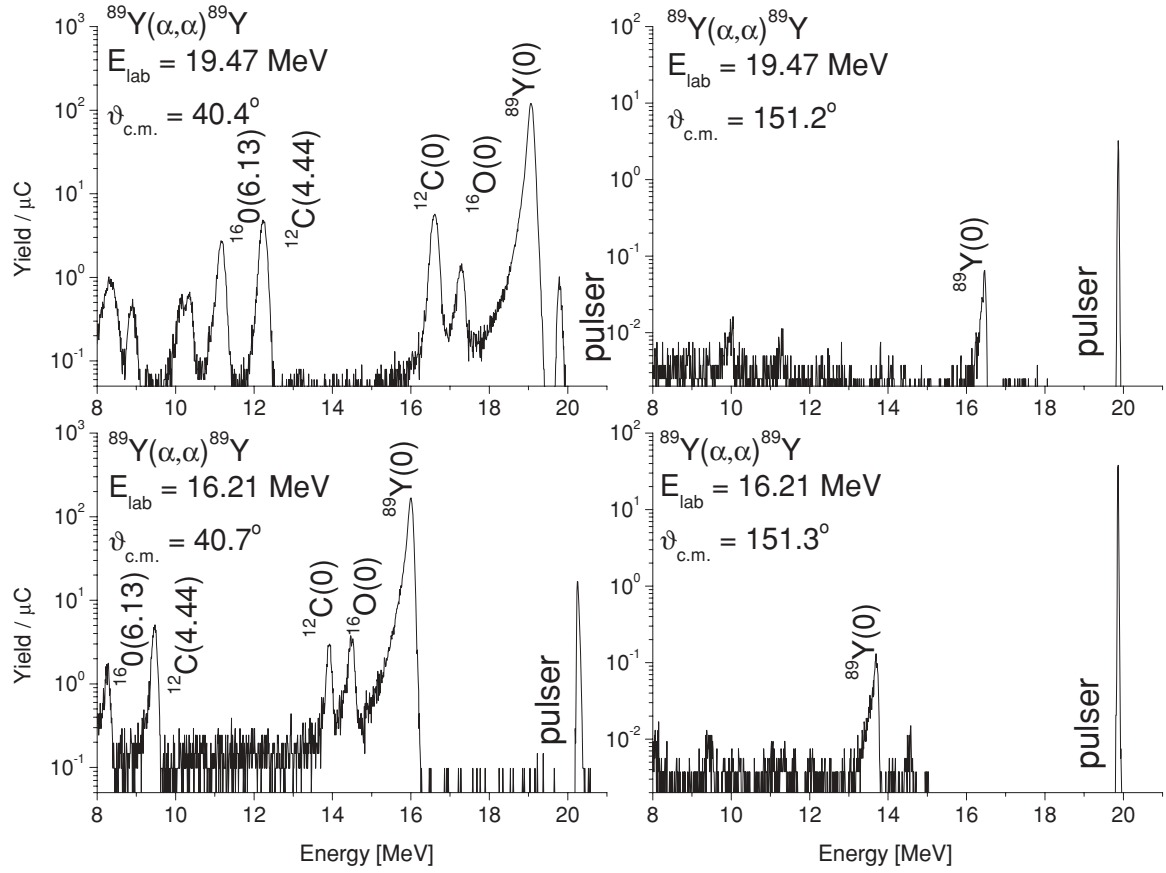

FIG. 1. Typical spectra at $E_{\text{c.m.}} = 15.51$ MeV and 18.63 MeV, $\vartheta_{\text{c.m.}} \approx 40^\circ$ and 150°. The peak from elastic ^{89}Y-α scattering is well resolved from both the ^{12}C-α and ^{16}O-α elastic scattering. The pulser peak used for the dead-time correction is also shown. Note the logarithmic scale of all spectra.

as monitor detectors during the experiment to normalize the measured angular distribution and to determine the precise position of the beam on the target. The solid angle of these detectors was $\Delta\Omega = 8.2 \times 10^{-6}$.

The signals from all detectors were processed using charge-sensitive preamplifiers. The output signals were further amplified by main amplifiers and fed into analog-to-digital converters. Because the elastic-scattering cross sections at forward angles differ several orders of magnitude from the one measured at backward angles, a reliable dead-time correction is crucial. The data were collected using the WinTMCA system that provides an automatic dead-time control. This automatically determined dead time was verified using a pulser in all spectra.

The energy of the first of the excited state of the ^{89}Y nucleus is 908.97 keV [21]. There is a large difference between the spin of the ground and the first excited states ($1/2^-$ and $9/2^+$ respectively). Therefore the expected inelastic scattering cross section is very low (below 10^{-4} mb, calculated with the DWUCK code [22]) at the measured energies. This fact explains why events corresponding to inelastic α scattering on ^{89}Y are missing from the spectra. Typical spectra are shown in Fig. 1. The relevant peaks from elastic ^{89}Y-α scattering are well separated from elastic and inelastic peaks of target contaminations, and—as expected—peaks from inelastic α scattering on ^{89}Y are not visible.

C. Angular calibration

Knowledge on the exact angular position of the detectors is of crucial importance for the precision of a scattering experiment because the Rutherford cross section depends sensitively on the angle. The uncertainty in the angular distribution is dominated by the error of the scattering angles in the forward region. A tiny uncertainty of $\Delta\vartheta = 0.3^\circ$ results in a significant error of approximately 5% in the Rutherford normalized cross sections at very forward angles.

To determine the scattering angle precisely, we measured kinematic coincidences between elastically scattered α particles and the corresponding ^{12}C recoil nuclei using a pure carbon foil target. One detector was placed at $\vartheta = 70^\circ$, and the signals from the elastically scattered α particles on ^{12}C were selected as gates for the other detector, which moved around the expected ^{12}C recoil angle $\vartheta = 45.85^\circ$. Figure 2 shows the relative yield of the ^{12}C recoil nuclei in coincidence with elastically scattered α particles as a function of the ^{12}C recoil angle. The final angular uncertainty was found to be $\Delta\vartheta \leqslant 0.15^\circ$.

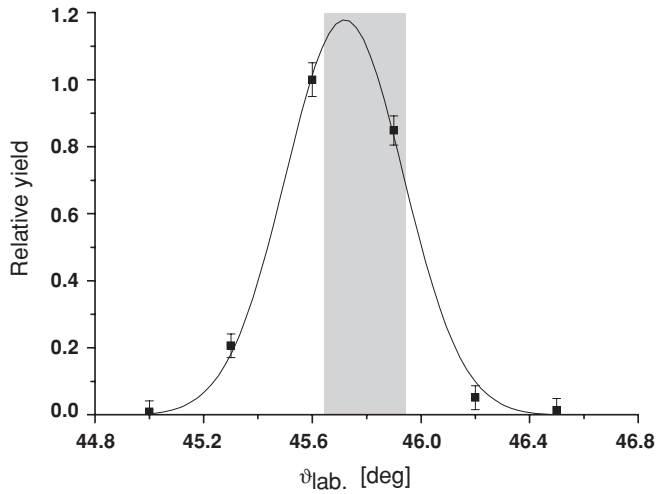

FIG. 2. Relative yield of ^{12}C recoil nuclei in coincidence with elastically scattered α particles. The shaded area represents the angle and uncertainties expected from the reaction kinematics. A Gaussian curve fitted to the experimental data is shown to guide the eye.

D. Elastic-scattering cross sections and data analysis

Complete angular distributions between 20° and 170° were measured at energies of $E_\alpha = 16.21$ and 19.47 MeV in 1° ($20° \leqslant \vartheta \leqslant 100°$), 1.5° ($100° \leqslant \vartheta \leqslant 140°$), and 2° ($140° \leqslant \vartheta \leqslant 170°$) steps.

The statistical uncertainties varied between 0.1% (forward angles) and 4% (backward angles). The count rates $N(\vartheta)$ have been normalized to the yield of the monitor detectors $N_{\text{Mon.}}(\vartheta = 15°)$:

$$\left(\frac{d\sigma}{d\Omega}\right)(\vartheta) = \left(\frac{d\sigma}{d\Omega}\right)_{\text{Mon.}} \frac{N(\vartheta)}{N_{\text{Mon.}}} \frac{\Delta\Omega_{\text{Mon.}}}{\Delta\Omega}, \tag{1}$$

with $\Delta\Omega$ being the solid angles of the detectors. The cross section at the position of the monitor detectors is taken as pure Rutherford. The relative measurement eliminates the typical uncertainties of absolute measurements, coming mainly from changes in target and from the beam current integration.

The measured angular distributions are shown on Fig. 3. The lines are the results from the local potential that is fitted to the experimental data. The measured absolute cross sections cover five orders of magnitude between the highest (forward angles at $E_\alpha = 16.21$ MeV) and the lowest cross sections (backward angle at $E_\alpha = 19.47$ MeV) with almost the same accuracy (4–5% total uncertainty). This error is mainly caused by the uncertainty of the determination of the scattering angle in the forward region and from the statistical uncertainty in the backward region.

III. LOCAL OPTICAL POTENTIAL AND α-CLUSTER STATES

A. Local folding potential

The complex optical model potential (OMP) is given by:

$$U(r) = V_C(r) + V(r) + iW(r), \tag{2}$$

where V_C(r) is the Coulomb potential, $V(r)$, and $W(r)$ are the real and the imaginary parts of the nuclear potential, respectively. The real part of the potential is calculated from the folding procedure [23,24] using a density-dependent nucleon-nucleon interaction. The calculated folding potential is adjusted to the experimental scattering data by two parameters

$$V(r) = \lambda V_F(r/w) \tag{3}$$

where $\lambda \approx 1.1$–1.4 is the potential strength parameter [7] and $w \approx 1.0 \pm 0.04$ is the width parameter that slightly modifies the potential width. (Larger deviations of the width parameter w from unity would indicate a failure of the folding potential.) The nuclear densities of ^{89}Y and α are derived from the measured charge density distributions [25]. For details of the folding potential see also [26,27].

The imaginary part $W(r)$ is taken in the usual Woods-Saxon parametrization. For the fits to the experimental data we use a sum of volume and surface potential:

$$W(r) = W_V \times f(x_V) + 4W_S \times \frac{df(x_S)}{dx_S} \tag{4}$$

with the potential depths W_V and W_S of the volume and surface parts and

$$f(x_i) = \frac{1}{1 + \exp(x_i)} \tag{5}$$

and $x_i = (r - R_i * A_T^{1/3})/a_i$ with the radius parameters R_i, the diffuseness parameters a_i, and $i = S, V$. The adjustment of the OMP parameters leads to an excellent description of the new experimental data (see Fig. 3). The parameters of the potentials are listed in Table I.

It has to be noted that the folding potential in the real part may be replaced by a Woods-Saxon potential. A similar quality of the fits can be obtained in this case. However, the

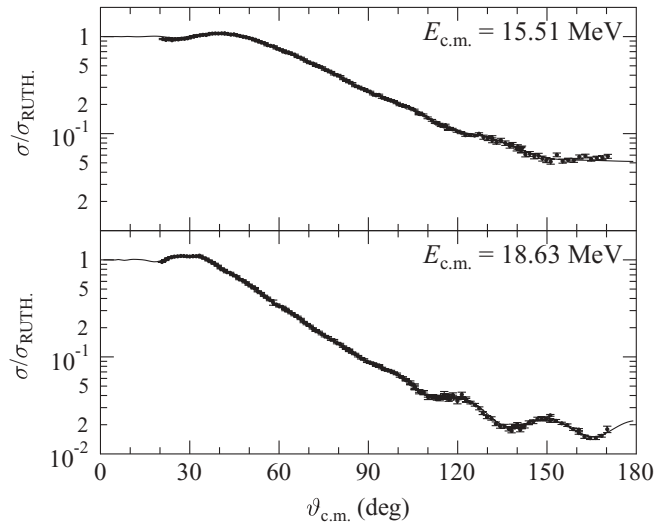

FIG. 3. Rutherford-normalized elastic-scattering cross sections of ^{89}Y(α,α)^{89}Y reaction at $E_{\text{c.m.}} = 15.51$ and 18.63 MeV versus the angle in center-of-mass frame. The lines are the results from the local potential that is fitted to the experimental data. The parameters of the fits are listed in Table I.

TABLE I. Parameters of the local potentials that were derived from elastic-scattering angular distributions in a wide energy range (see Figs. 3 and 4).

$E_{\mathrm{c.m.}}$ (MeV)	λ	w	J_R (MeV fm^3)	$r_{R,\mathrm{rms}}$ (fm)	J_I (MeV fm^3)	$r_{I,\mathrm{rms}}$ (fm)	W_{V0} (MeV)	R_V (fm)	a_V (fm)	$4 \times W_{S0}$ (MeV)	R_S (fm)	a_S (fm)	Experimental data from
15.5	1.350	0.986	342.3	4.905	49.9	5.953	−11.3	1.656	0.486	−8.3	1.350	0.548	This work
18.6	1.353	0.979	335.3	4.868	46.9	4.975	−20.0	1.331	0.713	−25.8	1.487	0.255	This work
20.1	1.328	0.985	334.9	4.897	45.0	5.262	−22.3	1.197	0.982	−55.7	1.501	0.174	Ref. [12]
22.0	1.352	0.969	324.7	4.817	47.2	5.856	−16.9	1.585	0.822	−42.7	1.460	0.502	Ref. [12]
23.9	1.315	0.989	335.8	4.917	46.6	4.955	−21.9	1.656	0.590	−71.2	1.435	0.605	Ref. [12]
23.9	1.326	0.984	334.5	4.896	44.7	4.735	−23.6	1.672	0.610	−78.5	1.423	0.678	Ref. [13]
40.2	1.268	1.002	328.0	4.988	57.5	5.672	−18.8	1.492	0.799	−26.3	1.475	0.429	Ref. [16]
62.2	1.296	1.007	328.3	5.016	65.6	5.835	−19.5	1.634	0.544	−56.7	1.388	0.365	Ref. [15]
158.9	1.317	0.985	260.0	4.930	82.3	5.785	−22.1	1.457	0.757	–	–	–	Ref. [14]

adjustment of three Woods-Saxon parameters in the real part and six parameters in the imaginary part leads to a variety of parameter sets with comparable χ^2. This problem was reduced in Ref. [4], where a microscopic Woods-Saxon potential was derived from a folding procedure. This potential is used as the base of one of the global potentials studied in Sec. IV.

The above calculation with folding potentials has been repeated for the ^{89}Y$(\alpha,\alpha)^{89}$Y scattering data available in literature from about 20 MeV up to about 170 MeV. The analyzed data have been measured by Brissaud *et al.* [14] at 166 MeV ($E_{\mathrm{c.m.}} = 158.9$ MeV), Bingham *et al.* [15] at 65 MeV ($E_{\mathrm{c.m.}} = 62.2$ MeV), Alster *et al.* [16] at 42 MeV ($E_{\mathrm{c.m.}} = 40.2$ MeV), England *et al.* [13] at 25 MeV ($E_{\mathrm{c.m.}} = 23.9$ MeV), and Wit *et al.* [12] at 25, 23, and 21 MeV ($E_{\mathrm{c.m.}} = 23.9, 22.0,$ and 20.1 MeV) with an additional excitation function at backward angles. The data measured by Berinde *et al.* [17] at 27.3 MeV ($E_{\mathrm{c.m.}} = 26.1$ MeV) were excluded because all fits were of poor quality and required width parameters w deviating strongly from unity. The new and challenging technique for the measurement of angular distributions using a position-sensitive detector in the work of Berinde *et al.* [17] was unfortunately not further developed; this may indicate that there are problems with the data of Ref. [17].

At 25 MeV two data sets are available. The data by England *et al.* [13] cover the whole angular range from forward to backward directions. As expected, at forward angles the data agree with the Rutherford cross section, and thus the uncertainty of the absolute normalization of the data is of the order of a few percentages. The data by Wit *et al.* [12] focus on the backward region and start around $\vartheta_{\mathrm{c.m.}} \approx 50^\circ$ where the cross section is about 20–30% of the Rutherford cross section. Although an uncertainty of about ±15% is claimed in Ref. [12], the comparison to the data by England *et al.* [13] shows that the data by Wit *et al.* have to be reduced by a factor of 1.45 to come into agreement with the England *et al.* data. The origin of this discrepancy remains unclear. Because typical normalization problems (e.g., uncertainties of the target thickness) apply probably to all measurements of the ^{89}Y$(\alpha,\alpha)^{89}$Y cross section in Ref. [12], we use the reduction factor of 1.45 for all data for ^{89}Y measured by Wit *et al.* [12], i.e., the three angular distributions at 21, 23, and 25 MeV and the excitation function at backward angles.

The calculated cross sections are compared to the experimental data in the broad energy range from about 20 MeV up to about 160 MeV in Fig. 4. Similar to the result for the new low-energy data shown in Fig. 3, excellent agreement is obtained for all angular distributions in the wide energy range

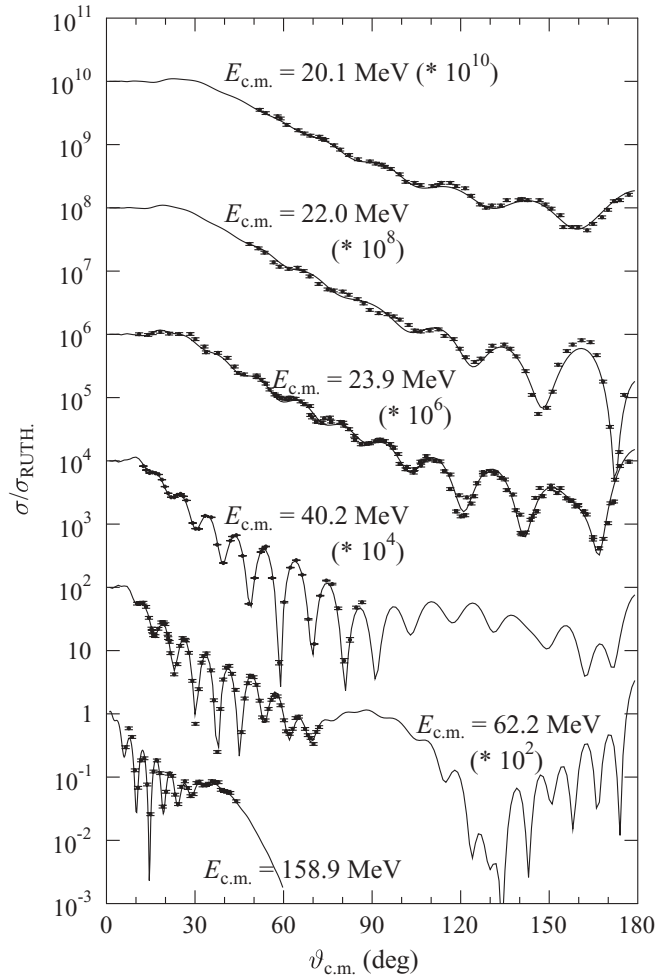

FIG. 4. Rutherford-normalized elastic-scattering cross sections of ^{89}Y$(\alpha,\alpha)^{89}$Y reaction at energies between 20 and 160 MeV. The experimental data are taken from the literature [12–16]. The parameters of the fits are listed in Table I.

from slightly above the Coulomb barrier up to 160 MeV. The parameters of the potential are also listed in Table I.

Unfortunately, the angular distributions at $E_{\text{c.m.}} =$ 40.2 MeV and 62.2 MeV do not cover the backward angular range which is most sensitive to the imaginary part of the potential. However, the derived potentials from the analysis of the England *et al.* data at 25 MeV and the corrected Wit *et al.* data at 25 MeV are in reasonable agreement; this indicates that the Wit *et al.* data that focus on the backward angular region are sufficient to derive the optical potential—provided that the absolute normalization is correct. In practice this means that data in the forward region are not necessary to derive the potential but are highly necessary to define the absolute normalization of the data by comparison to the Rutherford cross section.

The various available scattering data for ^{89}Y enable a study of the energy dependence of the potential parameters that are derived from the fits to the angular distributions in Figs. 3 and 4. For the real part a very smooth dependence of the strength parameter λ and the width parameter w is found; see Fig. 5. As expected, the width parameter w remains close to unity at all energies, and the strength parameter λ is almost energy independent and varies less than 10% between 1.27 and 1.35, leading to volume integrals J_R for the real part in agreement with the systematics of Ref. [7]. The much stronger decrease of the real volume integral J_R with energy by about 25% is

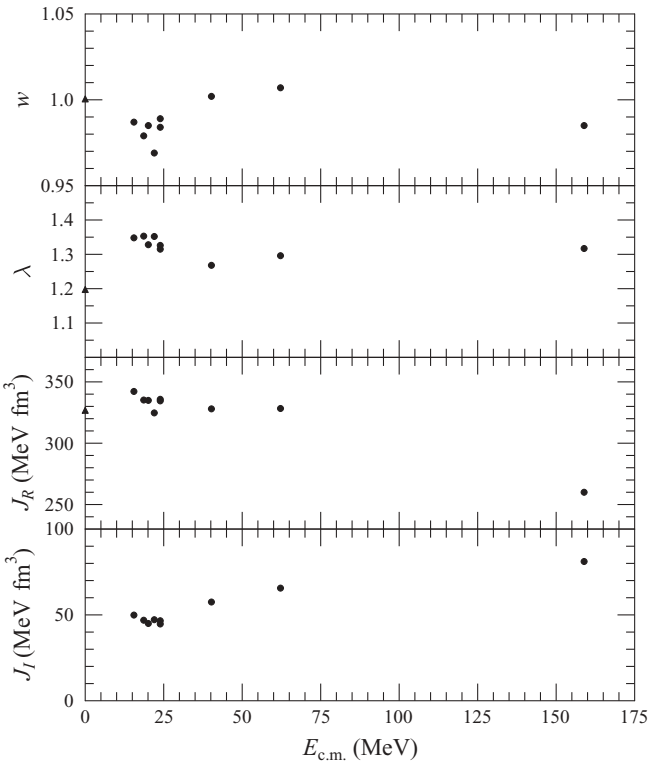

FIG. 5. Potential parameters λ and w and the integral potential strengths J_R and J_I for the real and imaginary part of the potentials that are derived from the fits to the angular distributions in Figs. 3 and 4 (full circles). Additionally, the result from the bound state adjustment in Sec. III B is shown with triangles at $E = 0$. Further discussion see text.

a consequence of the energy dependence of the interaction and the dispersion relation that couples the real and imaginary parts of the potential. [Note that (as usual) the negative sign of the volume integrals J_R and J_I is neglected in the discussion.]

The volume integral J_I of the imaginary part increases with energy, but it remains below $J_I = 100$ MeV fm^3, in agreement with the systematics shown in Ref. [7]. However, the slope of J_I vs. $E_{\text{c.m.}}$ is not well defined from the available data, particularly not in the low-energy region that is most relevant for nuclear astrophysics. All data between 15 MeV $\leqslant E_{\text{c.m.}} \leqslant$ 25 MeV lead to volume integrals of about $J_I \approx 50$ MeV fm^3. However, a closer look at the imaginary potentials shows that the shape of the potentials changes significantly between the different energies (see Fig. 6, lower part), which complicates the analysis of the $J_I(E)$ dependence. Contrary to the imaginary potentials, the shape of the real potentials is well defined from the folding procedure (see Fig. 6, upper part).

It has to be noted that there are discrete ambiguities for the real part of the OMP. This has been illustrated, e.g., in Fig. 5 of Ref. [11] where 11 "families" of potentials were identified that resulted in a similar description of the low-energy ^{144}Sm(α,α)^{144}Sm elastic-scattering data. However, these discrete ambiguities are significantly reduced in the present analysis because of the data at higher energies. It is not possible to describe the data at 62.2 and 158.9 MeV using potentials from another family, i.e., using a potential strength that is increased or decreased by about 30%.

Together with the determination of the bound state potential in Sec. III B, the family with $J_R \approx 320$–350 MeV fm^3 has been selected in the analysis of the low-energy scattering data. For completeness it has to be pointed out that the above volume integral of $J_R \approx 320$–350 MeV fm^3 at low energies is valid only for folding potentials. Slightly different numbers will

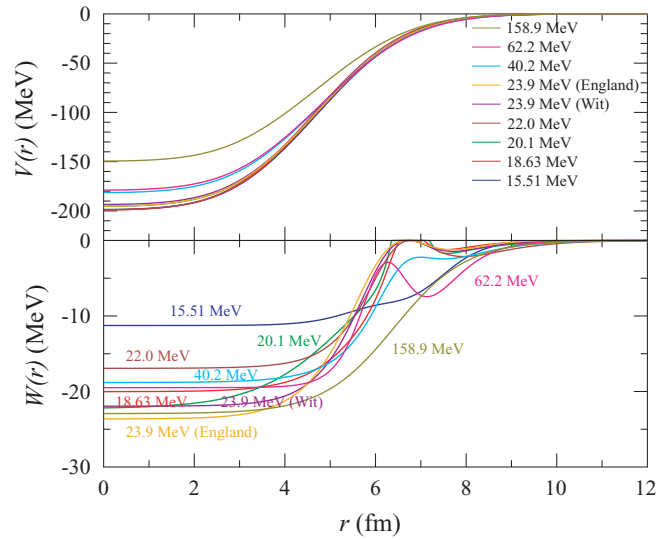

FIG. 6. (Color online) Shape of the potentials for the fits in Figs. 3 and 4. The upper part shows the very regular behavior of the real part $V(r)$. The lower part shows the variations of the shape of the imaginary potential $W(r)$ at the various energies. Further discussion see text.

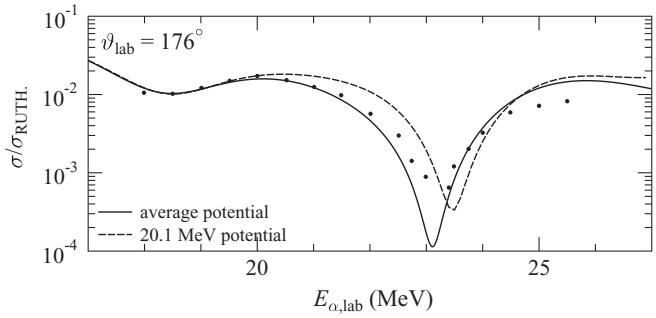

FIG. 7. Excitation function of ^{89}Y(α,α)^{89}Y at the angle $\vartheta_{lab} = 176^\circ$ [12] compared to calculations using the 20.1-MeV potential (dashed line) and an averaged potential from all fits below 25 MeV (full line).

be obtained if other parametrizations of the potential, e.g., Woods-Saxon potentials, are used (see, e.g., Ref. [3]).

In addition to the angular distributions, an excitation function at the very backward angle of $\vartheta_{lab} = 176^\circ$ has been measured in Ref. [12] in the energy range of 18 MeV $\leqslant E_{\alpha,lab} \leqslant$ 26 MeV, i.e., covering the energy range of the angular distributions in this work and in Refs. [12,13]. This excitation function has been calculated using the potential from the fit to the 20.1-MeV data from Ref. [12]; see Fig. 7. Additionally, an averaged potential has been calculated from all fits below 25 MeV. Both the 20.1-MeV potential and the average potential are able to reproduce the shape of the excitation function, including the deep minimum around 23 MeV; however, the agreement between theory and experiment is slightly worse for the excitation function at very backward angles (compared to the excellent reproduction of the angular distributions). Because of the relatively weak energy dependence of the volume integrals J_R and J_I below 25 MeV, this averaged potential will also be used for comparison with global potentials in Sec. IV.

B. α-cluster states in ^{93}Nb = ^{89}Y $\otimes$ α

α clustering in intermediate and heavy nuclei is a well-established phenomenon [7,28–30]. A link between the cluster model and the collective model has been discussed in Ref. [31], and it has been pointed out that a cluster model interpretation of collective properties—as recently reviewed in Ref. [32]—emerges.

The properties of α clustering above shell closures in the even-even nuclei ^{44}Ti = ^{40}Ca $\otimes$ α, ^{94}Mo = ^{90}Zr $\otimes$ α, and ^{212}Po = ^{208}Po $\otimes$ α have been studied extensively [7,28–30, 33–38]. However, only a few studies are available for even-odd nuclei below the above-mentioned shell closures [39–41]. Following the ideas in Refs. [39,40] for ^{43}Sc = ^{39}K $\otimes$ α, we analyze here α-cluster properties of ^{93}Nb = ^{89}Y $\otimes$ α. The ground state of ^{89}Y($Z = 39$, $N = 50$) has $J^\pi = 1/2^-$ that comes from a one-proton hole in the $p_{1/2}$ shell of the neighboring ^{90}Zr($Z = 40$, $N = 50$). Counterparts of the well-studied rotational bands in ^{94}Mo = ^{90}Zr $\otimes$ α should be found in ^{93}Nb = ^{89}Y $\otimes$ α with ^{89}Y = ^{90}Zr $\otimes$ $p_{1/2}^{-1}$. This study extends a recent review on α-cluster states in $N = 50$ $\otimes$ α even-even nuclei [42]. All excitation energies and decay properties of excited states in ^{93}Nb have been taken from Ref. [43].

The full formalism of the applied model can be found in, e.g., Refs. [7,38]. Here we briefly repeat the important features of the model. The α-cluster wave function can be directly calculated from the Schroedinger equation and the α-nucleus potential that is taken from the double-folding procedure (see also above). The so-called Wildermuth condition ensures that the Pauli principle is taken into account:

$$Q = 2N + L = \sum_{i=1}^{4}(2n_i + l_i) = \sum_{i=1}^{4} q_i, \qquad (6)$$

where Q is the number of oscillator quanta, N is the number of nodes, L is the relative angular momentum of the α-cluster wave function, and $q_i = 2n_i + l_i$ are the corresponding quantum numbers of the nucleons in the α cluster. We take $q = 4$ and thus $Q = 16$ for the $1/2^-$ band in ^{93}Nb = ^{89}Y($1/2^-$) $\otimes$ α. A $1/2^+$ band with $Q = 17$ should also exist in ^{93}Nb; however, no firm assignment could be found until now [43]. Also a higher nodal band with $Q = 18$ has not yet been found experimentally [43]. Typical properties of α-cluster states are large reduced widths θ_α^2 or spectroscopic factors. Unfortunately, no α transfer data like, e.g., (^{6}Li,d) on ^{89}Y can be found in Ref. [43]; such data have been essential for the assignment of α-cluster properties in many cases [44].

A prerequisite for a successful description of α-cluster states is an α-nucleus potential that is also able to describe the elastic α scattering cross section and/or α-decay properties (e.g., Refs. [28,38,39]). In the present investigation of ^{93}Nb we use a double-folding potential for the real part that is close to the result of the previous Sec. III A; the imaginary part of the potential vanishes at the very low energies studied here.

The properties of the α-cluster states in ^{93}Nb with a ^{89}Yb($1/2^-$) $\otimes$ α structure have been analyzed in the following way. In a first step the strength parameter λ of the double-folding potential is adjusted to reproduce the binding energy of the first $1/2^-$ state in ^{93}Nb; it is located at $E_x = 30.8$ keV or $E = Q_\alpha - E_x = -1900.7$ keV with the α binding energy $Q_\alpha = -1931.5$ keV. The result $\lambda = 1.1951$ and the corresponding volume integral $J_R = 326.1$ MeV fm^3 are very close to the numbers obtained from the analysis of the scattering data. For simplicity, the width parameter w has been fixed at $w = 1$ for the bound-state calculations.

For a perfect rotator the calculations with a realistic potential should be able to predict the energies of all members of this rotational band. However, it has been shown that the strength of folding potentials has to be slightly reduced with increasing angular momentum (or increasing excitation energy). It was found that an excellent description of the energies within rotational bands is obtained using a potential strength with a weak dependence on the angular momentum L:

$$\lambda(L) = \lambda(L = 0) - c \times L \qquad (7)$$

with small values for the constant $c \approx (3 - 5) \times 10^{-3}$ [34,39]. Thus, in a second step the potential strength was adjusted to the

TABLE II. Properties of the $Q = 16$, $K^\pi = 1/2^-$ rotational band in ^{93}Nb. For $L \geqslant 6$ only the centroid of the two states with $J = L \pm 1/2$ is given. Additionally the excitation energy of the $1/2^+$, $3/2^+$ band head of the $Q = 17$, $K^\pi = 1/2^+$ band is predicted.

L	J^π	Q	E (keV)	$E_x(^{93}\text{Nb})$ (keV)	λ
0	$1/2^-$	16	−1901	31[a]	1.1951[a]
2	$3/2^-$	16	−1244	687[a]	1.1856[a]
2	$5/2^-$	16	−1121	810[a]	1.1856[a]
4	$7/2^-$	16	−457	1474[b]	1.1761[b]
4	$9/2^-$	16	−238	1693[b]	1.1761[b]
6	$11/2^-, 13/2^-$	16	+613	2545[b]	1.1666[b]
8	$15/2^-, 17/2^-$	16	+1681	3613[b]	1.1571[b]
10	$19/2^-, 21/2^-$	16	+2878	4809[b]	1.1476[b]
12	$23/2^-, 25/2^-$	16	+4221	6152[b]	1.1381[b]
14	$27/2^-, 29/2^-$	16	+5749	7680[b]	1.1286[b]
16	$31/2^-, 33/2^-$	16	+7514	9445[b]	1.1191[b]
1	$1/2^+, 3/2^+$	17	+4765	6696[b]	1.1904[b]
0	$1/2^-$	18	+9432	11363[b]	1.1951[b]

[a] E from experimental data; λ adjusted to fit the energy E.
[b] E predicted using $\lambda(L) = \lambda(L = 0) - c \times L$, Eq. (7).

centroid of the $3/2^-$ and $5/2^-$ states with $L = 2$; we find $\lambda = 1.1856$ and derive $c = 4.75 \times 10^{-3}$ in excellent agreement with several other nuclei [39]. Then we use a weak spin-orbit potential $V_{LS} \sim 1/r \times dV_F/dr$; the strength of this spin-orbit potential is adjusted to reproduce the splitting of the $3/2^-$ and $5/2^-$ states with $L = 2$. Now all parameters of the potential are fixed, and it is possible to calculate the energies of the members of the $Q = 16$ rotational band in ^{93}Nb. The results are listed in Table II.

There are a number of candidates for the $L = 4$ states with $J^\pi = 7/2^-$ and $9/2^-$ at $E_x = 1364$ keV, 1500 keV, 1603 keV, and 1916 keV; however, no firm assignment is possible at the present stage. Therefore, for the higher-lying members of the rotational band with $L \geqslant 6$ only the centroid energy of the states with $J = L \pm 1/2$ are listed in Table II. In addition, the band heads of the $L =$ odd, $Q = 17$ and $L =$ even, $Q = 18$ bands are predicted.

The uncertainties of the predictions in Table II can be estimated from the uncertainty of the potential strength parameter $\lambda(L)$ and thus from the uncertainty of the constant c of about 20% [39]. The uncertainty of the potential strength $\lambda(L)$ in Eq. (7) increases with L from about 2×10^{-3} at $L = 4$ to about 0.01 around $L = 10$. The resulting uncertainty is of the order of about 150 keV for the $L = 4$ states and up to several hundred keV for states with higher angular momentum L. Together with an additional uncertainty from the weak spin-orbit potential of the order of 100 keV the total uncertainty for the predicted excitation energies is about 200 keV for the $L = 4$ states and larger for higher L. Slightly varying potentials have been used for the description of bands with different Q. This leads to an increased uncertainty of the order of 1 MeV for the band heads of the $Q = 17$ and $Q = 18$ rotational bands in ^{93}Nb.

Electromagnetic decay properties may provide additional hints for the α-cluster structure of the $Q = 16$ rotational band in ^{93}Nb. It is straightforward to calculate the wave functions of these states and the reduced transition strengths $B(E2, J_i^\pi \rightarrow J_f^\pi)$ for transitions from an initial state with J_i^π to a final state with J_f^π [46]. The results are listed in Table III. Indeed, enhanced transition strengths of the order of 10 W.u. are found for several transitions.

Experimental data for transition strengths are rare and have huge uncertainties. Within these uncertainties, the transition strengths for the transitions from the $L = 2$ states with $J_i^\pi = 3/2^-$ and $5/2^-$ to the final state with $L = 0$, $J_f^\pi = 1/2^-$ are calculated correctly.

For transitions from $L = 4$ states to $L = 2$ states predictions are given in Table III. It is interesting to note that the absolute transition strengths $\Gamma_{i \rightarrow f}$ depend sensitively on the predicted energies of these states because of the E_γ^5 dependence of $E2$ transitions. However, the reduced transition strengths are almost independent of the predicted energy. From the above-mentioned candidates for the $L = 4$ states, only the transition from the $J_i = 7/2$ state at $E_x = 1500$ keV to the $J_f^\pi = 5/2^-$ state at $E_x = 810$ keV has been detected experimentally. The preferred electromagnetic decay mode of most of the $L = 4$ candidates proceeds via $E1$ transitions to low-lying $J_f^\pi = 7/2^+$ and $9/2^+$ states that can be found at $E_x = 0$, 744, and 1083 keV. Thus, the predictions of $B(E2)$ values in Table III are not able to firmly assign the $L = 4$ members of the $Q = 16$ rotational band because of missing experimental data for weak decay branches. It has to be noted that a 1-MeV transition in ^{93}Nb with a $E1$ strength of 10^{-3} W.u. corresponds to $\Gamma_\gamma(E1) \approx 1.4$ meV, whereas a similar 1-MeV $E2$ transition with 10 W.u. corresponds to a much smaller radiation width of only $\Gamma_\gamma(E2) = 0.2$ meV.

In a recent article, the state at $E_x = 1500$ keV has been assigned $J^\pi = 9/2^-$ [48] instead of $J^\pi = 7/2^{(-)}$ [45,47], and

TABLE III. Calculated reduced transition strengths $B(E2)$ in the $Q = 16$, $K^\pi = 1/2^-$ rotational band in ^{93}Nb compared to experimental values [43].

L_i	J_i^π	$E_{x,i}$ (keV)	L_f	J_f^π	$E_{x,f}$ (keV)	$B(E2, J_i \rightarrow J_f)_{\text{calc}}$ (W.u.)	$B(E2, J_i \rightarrow J_f)_{\text{exp}}$ (W.u.)
2	$3/2^-$	687	0	$1/2^-$	31	8.6	11^{+35}_{-10}
2	$5/2^-$	810	0	$1/2^-$	31	8.6	<79
4	$7/2^-$	1474	2	$3/2^-$	687	10.7	–
4	$7/2^-$	1474	2	$5/2^-$	810	1.2	–
4	$9/2^-$	1693	2	$5/2^-$	810	12.0	–

an $E2$ transition strength of $26.4^{+9.7}_{-6.2}$ W.u. has been measured for the transition to the $5/2^-$ state at $E_x = 810$ keV [48]. A tiny readjustment of the potential strength parameter λ of about 0.2 % from the extrapolated value of 1.1761 to 1.1788 is required to shift the $9/2^-$ state from the predicted value $E_x = 1693$ to 1500 keV. Simultaneously, the $7/2^-$ state is shifted from the prediction $E_x = 1474$ to 1282 keV, which is very close to the $J^\pi = 5/2^-, 7/2^-$ state at $E_x = 1364$ keV. As pointed out above, the calculated transition strength of 12 W.u. for the $9/2^- \rightarrow 5/2^-$ $E2$ transition is practically independent of the precise excitation energies. The enhanced experimental transition strength confirms the $J^\pi = 9/2^-$ assignment of Ref. [48] for the $E_x = 1500$ keV state and the interpretation as a member of the $L = 4$ doublet with $^{89}\mathrm{Y} \otimes \alpha$ structure.

IV. GLOBAL OPTICAL MODEL PREDICTIONS

After the successful study of ^{89}Y$(\alpha,\alpha)^{89}$Y elastic scattering and $^{93}\mathrm{Nb} = {}^{89}\mathrm{Y} \otimes \alpha$ bound-state properties with a locally optimized potential we will now test the predictions of global α-nucleus optical potentials for the ^{89}Y$(\alpha,\alpha)^{89}$Y elastic-scattering cross section. Obviously, the best description of elastic-scattering data is obtained from a locally adjusted potential. However, such a locally optimized potential requires experimental data for adjustment that are often not available. In particular, for unstable nuclei it is not possible to measure elastic-scattering data with the required precision. Therefore global α-nucleus potentials are required for the prediction of scattering and reaction data. In the following we will compare the predictions of published global potentials to our experimental results.

The prediction of cross sections for unstable nuclei requires the extrapolation of global potentials into regions of the nuclear chart where no scattering data are available to test the extrapolations. It has been shown recently [10] that the variation of the potential along an isotopic chain (in that case $Z = 50$) can be sensitively studied by a comparison of the scattering cross sections of a neutron-rich and a neutron-deficient isotope. Here we extend this idea and study the variation of the scattering cross sections along the $N = 50$ isotonic chain by a comparison of scattering data for ^{89}Y and ^{92}Mo.

Several different parametrizations exist for the optical potential. For reactions involving α particles the optical potential is described mainly by complex Woods-Saxon potentials. Some authors investigated the use of higher-order terms of the Woods-Saxon function, too [49,50]. Model-independent parametrizations have also been studied, either with spline functions [49,51] or a series of Fourier-Bessel functions added to the Woods-Saxon parametrizations [52,53] or with a sum of Gaussians [50]. A folding model has been introduced by Kobos *et al.* [54]. In the framework of this model an energy- and density-dependent effective interaction—approximating the nonlocal exchange component by an empirical parametrization—was used to describe α-particle elastic scattering at energies from 25 to 120 MeV. This model was also extended for inelastic scattering. However, in all of these investigations the parametrization of the imaginary part of the optical potential varied from nucleus to nucleus to obtain a good description of the scattering cross sections for all the nuclei studied.

In the framework of the p process network calculations a large number of reactions involving α particles (α-induced reactions and α-particle emission) has to be taken into account. As the p-process path is located in a region of unstable nuclei on the neutron-deficient side of the chart of nuclides, experimental data are practically not available to adjust potential parameters of the α-nucleus potential. Therefore, a global α-nucleus optical potential is required for the theoretical prediction of reaction cross sections involving α particles within the statistical Hauser-Feshbach model.

Several different global and regional parametrizations have been developed in recent years to describe the interaction between nuclei and α particles. In the following an overview of the parametrizations is given that are studied in this work.

(i) The regional α-nucleus potential of Avrigeanu *et al.* [4] corresponds to average mass-, charge-, and energy-dependent Woods-Saxon parameters based on local potentials obtained by analysis of 108 experimental angular distributions of α-particle elastic scattering on target nuclei from ^{50}Ti to ^{124}Sn and α-particle energies from 8.1 to 49 MeV. The local Woods-Saxon parameter sets provided by the analysis of the new experimental data (Table 2 of Ref. [4]) have led to similar results as those shown in Fig. 3 (see also Fig. 7 of Ref. [4]).

(ii) The recently published global potential by Kumar *et al.* [5] claims to describe data in a wide mass ($12 \leqslant A \leqslant 209$) and energy region (from the Coulomb barrier up to 140 MeV); however, problems below 30 MeV had to be compensated by an enhanced imaginary volume integral, and even with this enhancement the description of ^{90}Zr$(\alpha,\alpha)^{90}$Zr scattering at 15 MeV is reasonable but not excellent (see Fig. 2 in Ref. [5]). A similar reproduction of the ^{89}Y$(\alpha,\alpha)^{89}$Y scattering data below 20 MeV is expected.

(iii) The widely used potential by McFadden and Satchler [59] is a very simple four-parameter Woods-Saxon potential with mass- and energy-independent parameters. Despite its simplicity it provides an excellent description of α-scattering data and cross sections of α-induced reactions; e.g., this potential is used as default for the Hauser-Feshbach calculations of astrophysical reaction rates by Rauscher and Thielemann [2,55].

Unfortunately, the latest version [56,57] of the potentials by Demetriou *et al.* [6] are published only in conference proceedings and cannot be used without the authors of Ref. [56,57]; we do not intend to show results from the early and perhaps outdated potentials in Ref. [6].

A. Angular distributions: comparison with theoretical models

The regional optical potential (ROP) of Avrigeanu *et al.* [3] was obtained by a semimicroscopic analysis, using the double folding model [58], based on α-particle elastic scattering on A

≈100 nuclei at energies below 32 MeV. The energy-dependent phenomenological imaginary part of this semimicroscopic optical potential takes into account also a dispersive correction to the microscopic real potential. A small revision of this ROP and especially the use of local parameter sets were able to describe the variation of the elastic-scattering cross sections along the Sn isotopic chain [18]. A further step to include all available α-induced reaction cross sections below the Coulomb barrier has recently been carried out [4]. First, the ROP based entirely on α-particle elastic scattering [3] was extended to $A \sim 50$–120 nuclei and energies from ~ 13 to 50 MeV. Second, an assessment of available (α, γ), (α, n), and (α, p) reaction cross sections on target nuclei ranging from ^{45}Sc to ^{118}Sn at incident energies below 12 MeV was carried out. In this work the most recent potential of Avrigeanu *et al.* [4] is used to calculate the scattering cross sections.

The potential from Kumar *et al.* [5] was proposed to describe α-induced reactions on $12 \leqslant A \leqslant 209$ target nuclei at $E \leqslant 140$ MeV. In that work, the systematics of volume integrals has been used to determine the real and the imaginary parts of the potential. The real potential volume integrals have been taken from the work of Atzrott *et al.* [7]. The best fit volume integrals from the phenomenological analysis, consistent with the above set, had been employed in their analysis. A similar approach was followed for the imaginary part starting with the volume integral systematics of the imaginary part. Moreover, at energies below 30 MeV a dispersive correction is taken into account. Calculations using this potential are able to reproduce the measured α-scattering angular distributions at higher energies [5]. Here we compare the predicted angular distributions from the Kumar *et al.* [5] potential to our new experimental data at lower energies close to the Coulomb barrier.

For completeness, we take into account also the potential of McFadden *et al.* [59]. Numerous α elastic-scattering experiments were done on nuclei between O and U at α energies of 24.7 MeV in the 60's. Fits were obtained using a four-parameter Woods-Saxon potential.

In Fig. 8 the measured angular distributions of the ^{89}Y$(\alpha,\alpha)^{89}$Y elastic α scattering at $E_{\text{c.m.}} = 15.51$ and $E_{\text{c.m.}} = 18.63$ MeV are shown. The different lines correspond to the predictions using the above discussed global and regional optical potential parametrizations without any further adjustment of parameters. The overall agreement between the calculations performed with using the potentials of Avrigeanu and McFadden and the experimental data is good. Only the calculation performed with the potential of Kumar *et al.* gives a significantly worse description of the experimental data. For a strict comparison between the potentials of Avrigeanu and McFadden a χ^2 analysis has been done. The resulting χ^2 parameters can be found in Table IV. As can be seen, the quality of the different parametrizations is similar although a value of $\chi^2_{\text{red}} \approx 1$ cannot be reached by any of the global potentials.

Our analysis is extended up to 23.9 MeV using the data of Wit *et al.* [12] and England *et al.* [13]. The ^{89}Y$(\alpha,\alpha)^{89}$Y elastic scattering was studied by Wit *et al.* at $E_{\text{c.m.}} \approx 20.1$, 22.4, and 23.9 MeV and by England *et al.* at $E_{\text{c.m.}} \approx 23.9$ MeV. Note that we have applied the same reduction of a factor of 1.45 to all experimental data on ^{89}Y in the Wit *et al.* article [12] (see Sec. III).

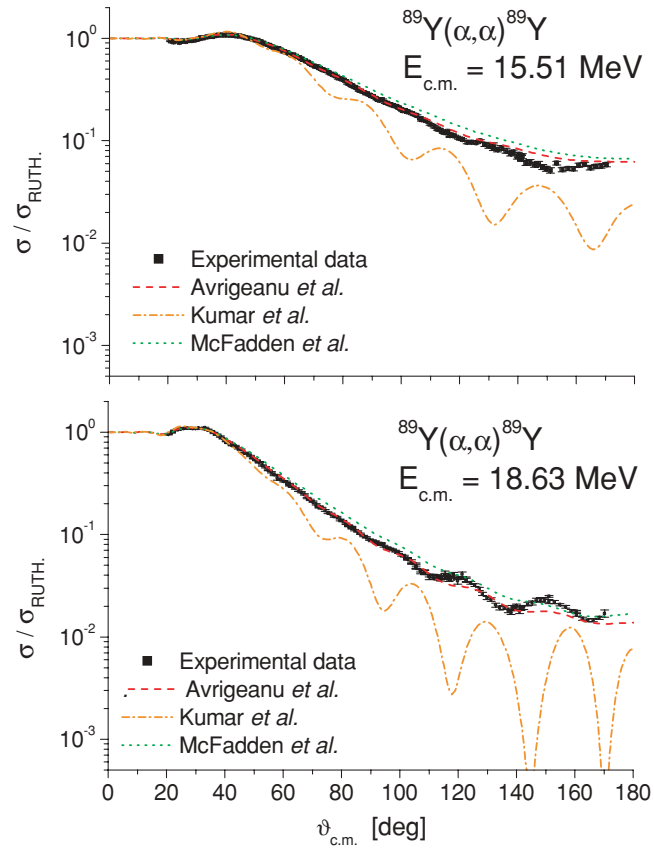

FIG. 8. (Color online) Rutherford-normalized elastic-scattering cross sections of ^{89}Y$(\alpha,\alpha)^{89}$Y reaction at $E_{\text{c.m.}} = 15.51$ and 18.63 MeV versus the angle in center-of-mass frame. The lines correspond to the predictions using different global optical potential parameter sets. For more information see Sec. IV.

In general, both the Avrigeanu and McFadden parametrizations can describe roughly both the magnitude and the oscillation pattern of the angular distributions measured at energies between 20.1 and 23.9 MeV. The calculations performed with the Kumar potential overestimate the strength of the oscillation, predicting deeper minima at backward angles. In the case of calculations performed with the other two

TABLE IV. χ^2_{red} of predictions using different global parametrizations compared with the angular distributions derived in the present work. No parameters have been adjusted to the new experimental data.

Global parameterizations	χ^2		Ref.
	15.51 MeV	18.63 MeV	
Avrigeanu	6.5	5.5	[4]
Kumar	181	287	[5]
McFaddden	35.3	40.9	[59]

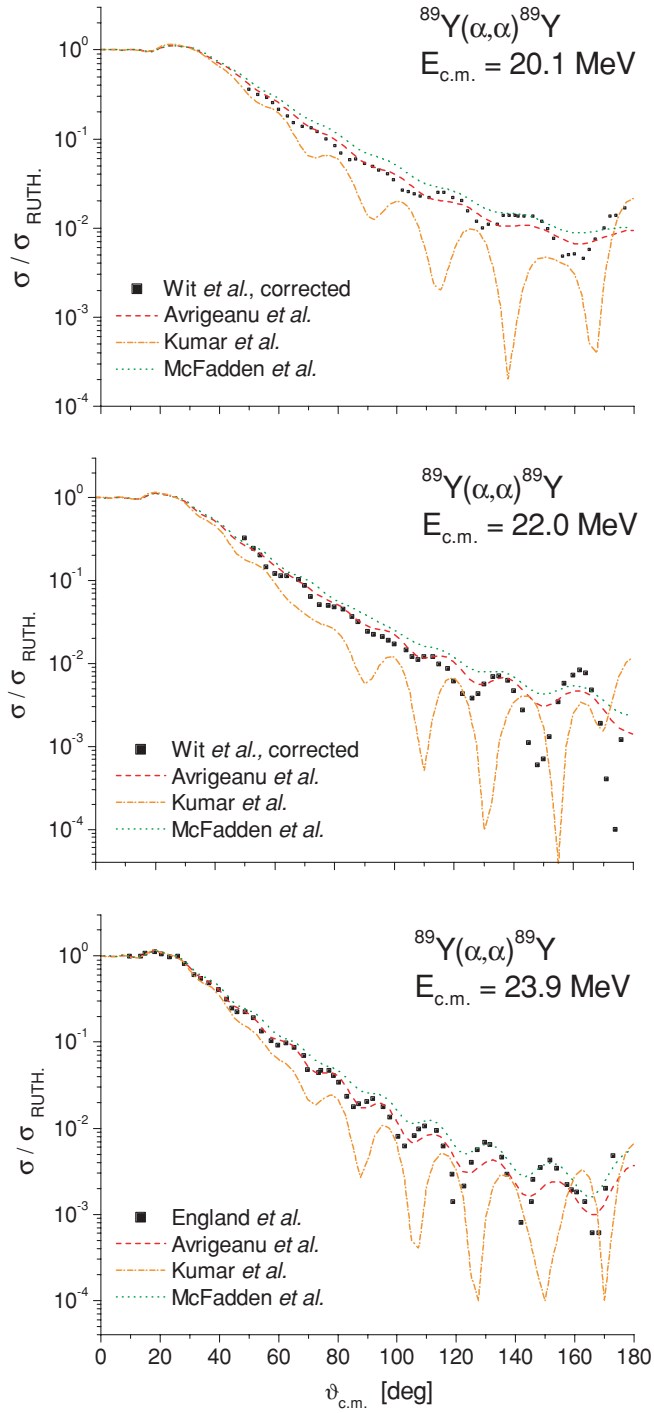

FIG. 9. (Color online) Rutherford-normalized elastic-scattering cross sections of ^{89}Y(α,α)^{89}Y reaction at $E_{\mathrm{c.m.}} = 20.1, 22.4$, and 23.9 MeV versus the angle in center-of-mass frame taken from Wit *et al.* and England *et al.* [12,13]. The data by Wit *et al.* [12] have been corrected by a factor of 1.45 to come into agreement with the England *et al.* data [13] at 23.9 MeV. The lines correspond to the predictions using different global optical potential parameter sets. For more information see Sec. IV.

global parametrizations slight differences at backward angles between the measured and calculated data can be seen in Fig. 9.

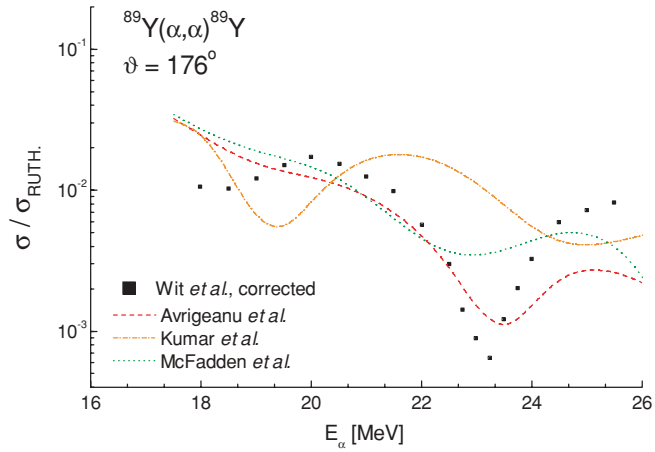

FIG. 10. (Color online) Excitation functions for elastic α scattering on ^{89}Y target nuclei at a scattering angle of 176° taken from the literature [12] and corrected by a factor of 1.45 (see text in Sec. IV A). The different curves correspond to the predictions using different global and regional potentials. For more information see Sec. IV.

B. Excitation functions

A perfect global optical potential should be able to predict angular distributions, including the diffraction-like patterns that show up at backward angles with increasing energy. It has to be pointed out that the backward angular region has a higher sensitivity to the optical potential than the forward angular region where the Coulomb interaction dominates. For a particular study of this backward angular region, an excitation function has been measured by Wit *et al.* [12] at $\vartheta = 176°$.

The measured excitation function of α-particle elastic scattering on ^{89}Y at a scattering angle 176° [12] and the corresponding optical model calculations using the potential from Avrigeanu *et al.* [4], Kumar *et al.* [5], and McFadden and Satchler [59] are shown in Fig. 10. Although there is reasonable agreement with the magnitude of the cross section in all calculations, the global potentials are not able to reproduce the energy dependence of the cross section. The sharp minimum of the experimental excitation function around 23 MeV is rather well described by the potential of Avrigeanu *et al.* [4], suggested by the global potential of McFadden and Satchler, and not predicted by the Kumar *et al.* global potential. The appropriate description of particular features of the experimental elastic scattering of α particles on ^{89}Y proves conclusively the suitable account of the nuclear absorption merely by the potential of Avrigeanu *et al.* However, the small scattering cross section at very backward angles (in particular in the pronounced minimum around 23 MeV in the excitation function, see Fig. 7) may be affected by small compound contributions [60]. Thus, minor deviations between the experimental and calculated cross sections are acceptable.

C. Comparison of global and local potentials

For further improvement of the global α-nucleus potentials a deeper understanding of the differences between the potentials and the resulting cross sections is required. In

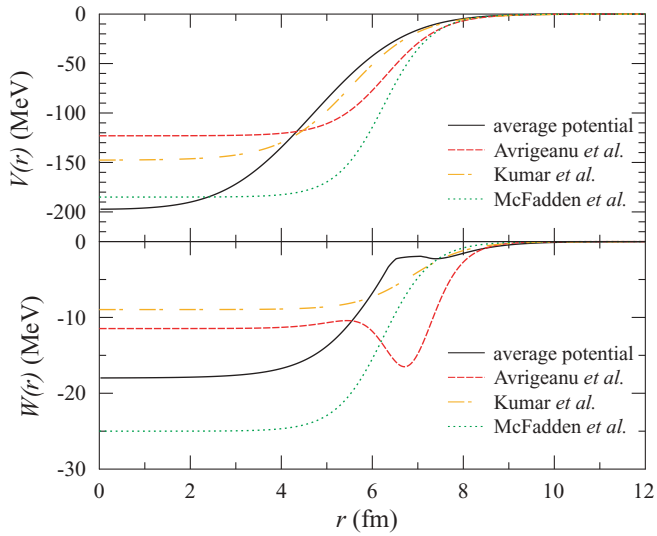

FIG. 11. (Color online) Comparison between the averaged local potential (see Sec. III A) and the global parametrizations at 18.63 MeV (see Sec. IV).

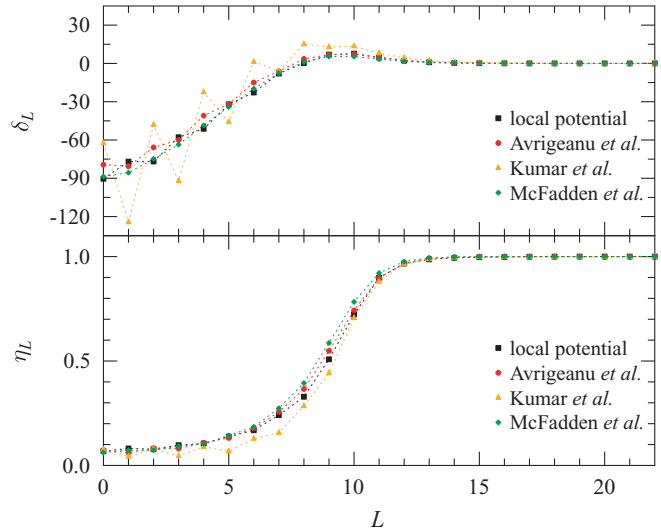

FIG. 12. (Color online) Comparison between the local potential (see Sec. III A) and the global parametrizations (see Sec. IV) for $E = 18.63$ MeV: elastic-scattering phase shift δ_L (upper) and amplitude of the scattered wave η_L (lower) in dependence of the angular momentum L. The data points are connected by dashed lines to guide the eye. Note that the scale in L with $0 \leqslant L \leqslant 22$ corresponds roughly the scale in r of Fig. 11 with $0 \leqslant r \leqslant 12$ fm according to Eq. (8).

the following paragraphs we will compare the shapes of the different potentials and the elastic phase shifts δ_L and scattered wave amplitudes η_L that define the elastic-scattering cross section. Note that the scattering cross section is related to the sum of the absolute squares over all contributing partial waves; the study of the underlying δ_L and η_L will allow a better understanding of the global potentials. However, it is beyond the scope of the present article to derive a new and improved global α-nucleus potential.

The shapes of the real and imaginary part of the local potential have already been shown in Fig. 6. Because of the minor energy dependence of the volume integrals J_R and J_I below 30 MeV (see Fig. 5), an averaged local potential is used for comparison to the global potentials. The global potentials are shown in Fig. 11. Huge differences can be seen for small radii, i.e., the nuclear interior, whereas at larger radii ($r > 8$ fm) all potentials are close to each other.

In a semiclassical picture larger radii in the potential correspond to larger impact parameters that are related to the angular momentum $\vec{L} = \vec{r} \times \vec{p}$. For example, for the energy $E = 18.63$ MeV this leads to the approximate relation

$$|\vec{L}|/\hbar \approx 1.85 \times r/\text{fm}. \tag{8}$$

As expected, the scattering phase shifts δ_L and scattered wave amplitudes η_L are in agreement for $L \gtrsim 15$ (see Fig. 12). However, the nuclear potential is relatively weak at such large radii, and thus the phase shifts δ_L are small and $\eta_L \approx 1$ (no absorption); the scattering cross section is dominated by the Coulomb interaction.

The situation changes for smaller angular momenta. Around $L \approx 10$ (or semiclassically, $r \approx 5.4$ fm) the decreasing η_L indicate increasing absorption. Simultaneously, the δ_L start to deviate from zero. For small $L \leqslant 5$ (corresponding $r \leqslant 2.7$ fm) the η_L values are coming close to zero, i.e., full absorption of the respective partial wave. For these partial waves the calculated phase shift δ_L does not have strong impact on the scattering cross section. In other words, the elastic-scattering cross section is not very sensitive to the potential at small radii. However, one should keep in mind that this simple semiclassical interpretation is not strictly valid; the determination of δ_L and η_L from the solution of the Schrödinger equation depends on the underlying real and imaginary potentials $V(r)$ and $W(r)$ for the whole range in r where $V(r)$ or $W(r)$ deviate from zero.

From Fig. 12 it can be seen that the potential by Avrigeanu *et al.* provides δ_L and η_L that are close to the result of the local analysis (which is taken as a reference here) for all L. In particular, the most relevant partial waves around $L \approx 10$ are nicely reproduced. The McFadden/Satchler potential leads to slightly but systematically larger values of η_L for the most relevant L around $L \approx 10$. This weaker absorption of the McFadden/Satchler potential can also be seen in Figs. 8 and 9 where the calculated cross section in the backward region overestimates the experimental data. The phase shifts for small L are best reproduced by McFadden/Satchler; however, as pointed out above, the scattering cross section is not very sensitive to this region. (This may be different for the calculation of α-induced reaction cross sections where the McFadden/Satchler potential has been used very successfully!) The predictions of δ_L and η_L from the Kumar *et al.* potential deviate significantly from the results of the local potential, and consequently the calculated scattering cross sections are not in good agreement with the experimental data.

D. Variation of the scattering cross section along $N = 50$ isotonic chain

Because modeling explosive nucleosynthesis scenarios requires reaction rates on large number of reactions involving

thousands of nuclei, the α-nucleus potential has to be known in a wide region. The reliability of the extrapolation to unstable nuclei can be tested by measuring the elastic-scattering cross sections on several nuclei along isotopic and isotonic chains. The ratio of Rutherford normalized cross sections along isotopic or isotonic chains is a very sensitive observable for the quality of α-nucleus potentials that was not taken into account in most previous studies. This interesting feature was not observed in earlier work because the backward angular range was usually not measured with sufficient accuracy.

The ^{92}Mo$(\alpha,\alpha)^{92}$Mo reaction has been investigated by Fülöp *et al.* at $E_{\text{c.m.}} = 13.20, 15.69$, and 18.62 MeV [8]. For completeness, in Fig. 13 the angular distributions of elastically scattered α particles on ^{92}Mo measured at $E_{\text{c.m.}} =$ 15.69, 18.62 MeV are shown. The different lines correspond to theoretical cross sections calculated from the above discussed global α nucleus potentials, again without any further adjustment of parameters. As can be seen, the situation is similar to the one found in the case of ^{89}Y$(\alpha,\alpha)^{89}$Y. Namely, the Avrigeanu and McFadden global parametrizations can describe the measured angular distributions with similar quality and the potential of Kumar fails to reproduce the experimental data.

To investigate the behavior of the optical potential parameters along the $N = 50$ isotonic chain we derived the ratio of the elastic-scattering cross sections of ^{92}Mo and ^{89}Y that are both neutron-magic nuclei. It is found that the normalized elastic α-scattering cross sections of ^{89}Y and ^{92}Mo differ by roughly 50–70% at backward angles, and the ratio shows a pronounced oscillation pattern. The large number of experimental points and the low uncertainties on both data sets provide a unique probe to understand the evolution of the α-nucleus potential along the $N = 50$ isotonic chain.

In Fig. 14 the experimental ratio of the Rutherford normalized elastic-scattering cross sections is compared to the corresponding results of the recent potential of Avrigeanu *et al.* [4], the most recent global OMP from Kumar *et al.* [5], and the well-known potential of McFadden and Satchler [59]. It can be clearly seen that no global parametrization

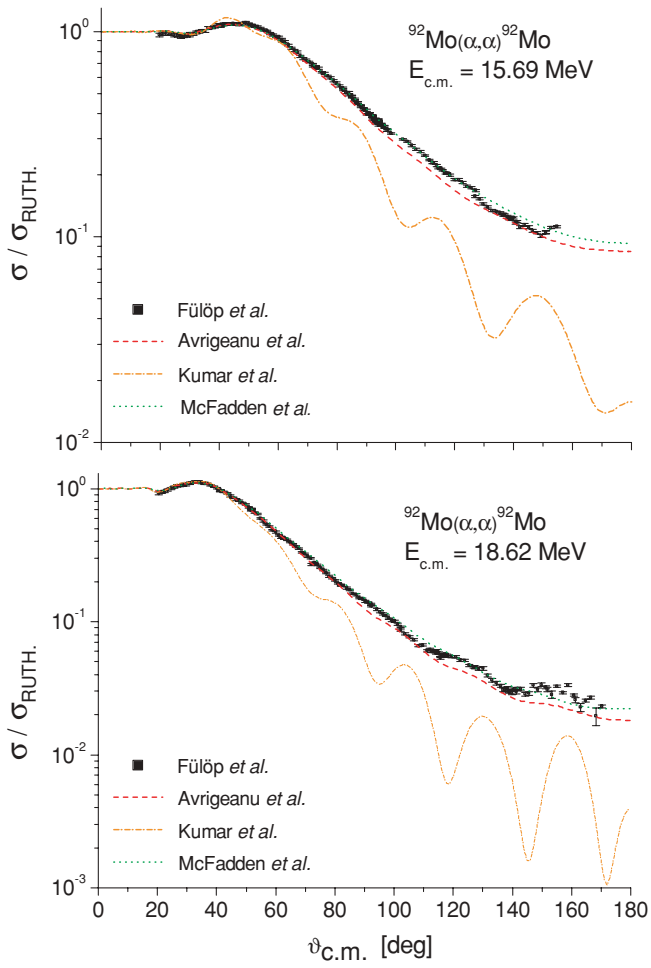

FIG. 13. (Color online) Rutherford-normalized elastic-scattering cross sections of ^{92}Mo$(\alpha,\alpha)^{92}$Mo reaction at $E_{\text{c.m.}} = 15.69$ and 18.63 MeV versus the angle in center-of-mass frame taken from Fülöp *et al.* [8]. The lines correspond to the predictions using different global optical potential parameter sets. For more information see Sec. IV.

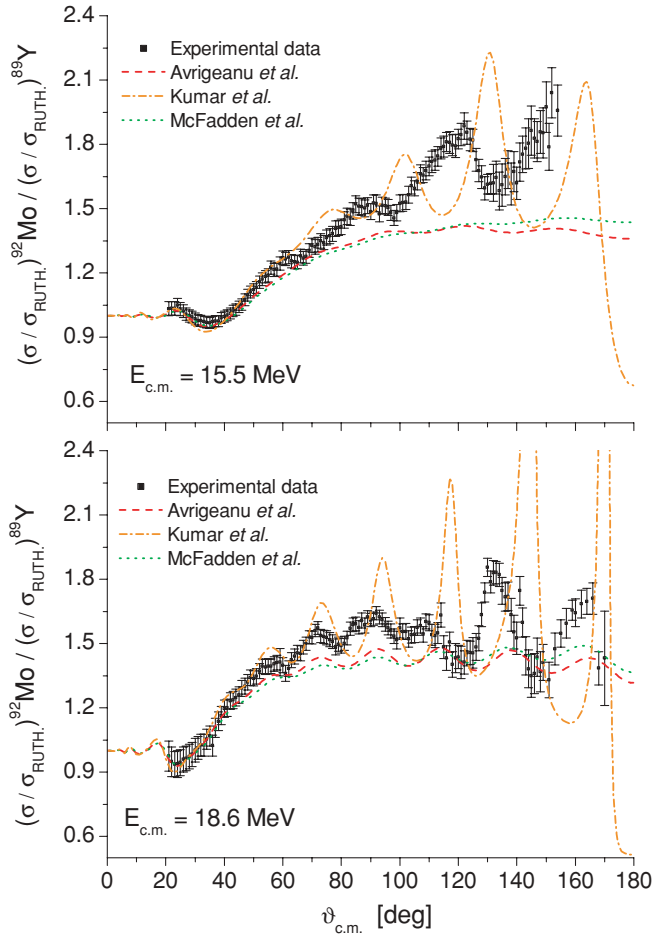

FIG. 14. (Color online) Experimental ratio of the scattering cross sections $(\sigma/\sigma_{\text{RUTH}})^{92}\text{Mo}/(\sigma/\sigma_{\text{RUTH}})^{89}\text{Y}$ at $E_{\text{c.m.}} \approx 15.51$ and 18.63 MeV versus the angle in center-of-mass frame. The cross sections of the ^{92}Mo$(\alpha,\alpha)^{92}$Mo are taken from Ref. [8]. The lines correspond to the predictions using different global optical potential parameter sets. For more information see Sec. IV.

can describe correctly the amplitude and the phase of the oscillation pattern of the experimental data at backward angles. This new observable may provide constraints for the further improvement of global α-nucleus potentials.

It may be added that, while the ROP [4] reproduces only the phase of oscillations rather well, the local Woods-Saxon parameter sets corresponding to these target nuclei and incident energies (Table 2 of Ref. [4]) provide a good description of this ratio at 15 MeV and a reasonable one at 19 MeV. Therefore, taking into account the ROP averaging nature, one may conclude that the difference between the experimental ratio values and those provided by the ROP describes the variance for particular nuclei with respect to the average behavior.

Recently, a similar study has been performed by Galaviz *et al.* [10] where the variation of the elastic-scattering cross sections along the tin isotopic chain had been studied. Complete angular distributions of the ^{112,124}Sn$(\alpha,\alpha)^{112,124}$Sn reactions at 18.8 MeV were measured. It was found that the elastic α-scattering cross sections of the ^{112}Sn and ^{124}Sn differ by roughly 30–40% at backward angles, and the ratio of the measured cross sections shows a similar oscillation feature. It became evident that the global α-nucleus potentials failed to reproduce either the strength or the oscillation pattern for backward angles [10]. This behavior is very similar to the ratio of the Rutherford normalized cross sections of the ^{92}Mo$(\alpha,\alpha)^{92}$Mo and ^{89}Y$(\alpha,\alpha)^{89}$Y derived in the present work. This fact clearly indicates that the available theoretical α-nucleus optical potential parametrizations have to be improved to be able to describe the variation of the angular distributions simultaneously along isotopic and isotonic chains. This is particularly important for the extrapolation into regions of the chat of nuclides where no scattering data exist.

V. SUMMARY

In the present work angular distributions of elastically scattered α particles on ^{89}Y have been measured at $E_{\text{c.m.}} =$ 15.51 and 18.63 MeV. The new experimental data have been used to determine the parameters of a locally optimized folding potential. To investigate the energy dependence of the potential parameters, angular distributions of ^{89}Y$(\alpha,\alpha)^{89}$Y elastic scattering at higher energies [12–16] have also been analyzed. The volume integrals of the local potential show a smooth variation with energy over a broad energy range. However, the shape of the imaginary potential cannot be strictly fixed at low energies.

In addition, the local potential is also used to study bound-state parameters of the $^{93}\text{Nb} = {}^{89}\text{Y} \otimes \alpha$ system. Excitation energies of excited states in ^{93}Nb and their decay properties can be described successfully with potential parameters very close to the scattering potential.

The new experimental scattering data have also been used as a sensitive test for global parametrizations of the α-nucleus potential that have to be used in p process network calculations. Obviously, the best description of the experimental data is obtained from the local potential where the parameters are fitted to reproduce the measured angular distributions. However, it is found that the global parametrizations of Refs. [4,59] also provide a good description for the measured angular distributions, and reasonable agreement has been found for the angular distributions at slightly higher energies that are available from the literature [12,13]. For a deeper understanding of the differences between the locally optimized potential and the global α-nucleus potentials, the calculated elastic phase shifts δ_L and scattered wave amplitudes η_L are presented.

Furthermore, the variation of elastic-scattering angular distributions along the $N = 50$ isotonic chain has been analyzed. Here all global parametrizations failed to reproduce the amplitude and/or phase of the oscillations of the ratio of the Rutherford normalized cross sections. To advance our current understanding of the α-nucleus optical potential, further experimental scattering data with high precision are essential as well as improvements of the available global α-nucleus potentials.

ACKNOWLEDGMENTS

We thank for A. Kumar for providing optical model calculations by using the optical potential of Ref. [5] for us. This work was supported by OTKA (K068801, T049245), by the European Research Council Grant agreement No. 203175, and DFG (SFB634 and ZI510/5-1). G.G. Kiss and D. Galaviz acknowledge the support of the Spanish CICYT under the project FPA2005-02379 and MEC Consolider project CSD2007-00042. Gy. Gyürky acknowledges support from the Bolyai grant. D. Galaviz acknowledges support by the Juan de la Cierva program of the Spanish Ministry of Science.

[1] M. Arnould and S. Goriely, Phys. Rep. **384**, 1 (2003).
[2] T. Rauscher and F.-K. Thielemann, At. Data Nucl. Data Tables **79**, 47 (2001).
[3] M. Avrigeanu, W. von Oertzen, A. J. M. Plompen, and V. Avrigeanu, Nucl. Phys. **A723**, 104 (2003); M. Avrigeanu, W. von Oertzen, and V. Avrigeanu, *ibid.* **A764**, 246 (2006).
[4] M. Avrigeanu, W. von Oertzen, A. Obreja, F. L. Roman, and V. Avrigeanu, At. Data Nucl. Data Tables **95**, 501 (2009).
[5] A. Kumar, S. Kailas, S. Rathi, and K. Mahata, Nucl. Phys. **A776**, 105 (2006).
[6] P. Demetriou, C. Grama, and S. Goriely, Nucl. Phys. **A707**, 253 (2002).
[7] U. Atzrott, P. Mohr, H. Abele, C. Hillenmayer, and G. Staudt, Phys. Rev. C **53**, 1336 (1996).
[8] Zs. Fülöp, Gy. Gyürky, Z. Máté, E. Somorjai, L. Zolnai, D. Galaviz, M. Babilon, P. Mohr, A. Zilges, T. Rauscher, H. Oberhummer, and G. Staudt, Phys. Rev. C **64**, 065805 (2001).
[9] G. G. Kiss, Zs. Fülöp, Gy. Gyürky, Z. Máté, E. Somorjai, D. Galaviz, A. Kretschmer, K. Sonnabend, and A. Zilges, Eur. Phys. J. **27**, 197 (2006).
[10] D. Galaviz, Zs. Fülöp, Gy. Gyürky, Z. Máté, P. Mohr, T. Rauscher, E. Somorjai, and A. Zilges, Phys. Rev. C **71**, 065802 (2005).

[11] P. Mohr, T. Rauscher, H. Oberhummer, Z. Máté, Zs. Fülöp, E. Somorjai, M. Jaeger, and G. Staudt, Phys. Rev. C **55**, 1523 (1997).
[12] M. Wit, J. Schiele, K. A. Eberhard, and J. P. Schiffer, Phys. Rev. C **12**, 1447 (1975).
[13] J. B. A. England, S. Baird, D. H. Newton, T. Picazo, E. C. Pollacco, G. J. Pyle, P. M. Rolph, J. Alabau, E. Casal, and A. Garci, Nucl. Phys. **A388**, 573 (1982).
[14] I. Brissaud, Y. Le Bornex, B. Tatischeff, L. Bimbot, M. K. Brussel, and G. Duhamel, Nucl. Phys. **A191**, 145 (1972).
[15] C. R. Bingham, M. L. Halbert, and A. R. Quinton, Phys. Rev. **180**, 1197 (1969).
[16] J. Alster, D. C. Shreve, and R. J. Peterson, Phys. Rev. **144**, 999 (1966).
[17] A. Berinde, I. Boca, D. Bucurescu, G. Constantinescu, C. Hategan, S. Hoppenau, M. Ivascu, N. Tufoi, and V. Zoran, Nucl. Instrum. Methods Phys. Res. **167**, 439 (1979).
[18] M. Avrigeanu and V. Avrigeanu, Phys. Rev. C **73**, 038801 (2006).
[19] B. D. Watson, D. Robson, D. D. Tolbert, and R. H. Davis, Phys. Rev. C **4**, 2240 (1971).
[20] Z. Máté, S. Szilágyi, L. Zolnai, Å. Bredbacka, M. Brenner, K.-M. Källmann, and P. Manngård, Acta Phys. Hung. **65**, 287 (1989).
[21] B. Singh, Nucl. Data Sheets **85**, 1 (1998).
[22] P. D. Kunz, DWUCK: A Disorted-Wave Born Approximation Program, 1996 (unpublished); http://spot.colorado.edu/∼kunz.
[23] A. M. Kobos, B. A. Brown, R. Lindsay, and G. R. Satchler, Nucl. Phys. **A425**, 205 (1984).
[24] G. R. Satchler and W. G. Love, Phys. Rep. **55**, 183 (1979).
[25] H. de Vries, C. W. de Jager, and C. de Vries, At. Data Nucl. Data Tables **36**, 495 (1987).
[26] H. Abele and G. Staudt, Phys. Rev. C **47**, 742 (1993).
[27] P. Mohr, T. Rauscher, H. Oberhummer, Z. Máté, Zs. Fülöp, E. Somorjai, M. Jaeger, and G. Staudt, Phys. Rev. C **55**, 1523 (1997).
[28] B. Buck, A. C. Merchant, and S. M. Perez, Phys. Rev. C **51**, 559 (1995).
[29] S. Ohkubo, Phys. Rev. Lett. **74**, 2176 (1995).
[30] S. Ohkubo, M. Fujiwara, and P. E. Hodgson, Prog. Theor. Phys. Suppl. **132**, 1 (1998).
[31] B. Buck, A. C. Merchant, S. M. Perez, and H. E. Seals, Phys. Rev. C **76**, 014310 (2007).
[32] R. F. Casten and E. A. McCutchan, J. Phys. G **34**, R285 (2007).
[33] B. Buck, J. C. Johnston, A. C. Merchant, and S. M. Perez, Phys. Rev. C **52**, 1840 (1995).
[34] S. Ohkubo, Y. Hirabayashi, and T. Sakuda, Phys. Rev. C **57**, 2760 (1998).
[35] F. Michel, G. Reidemeister, and S. Ohkubo, Phys. Rev. C **61**, 041601(R) (2000).
[36] B. Buck, J. C. Johnston, A. C. Merchant, and S. M. Perez, Phys. Rev. C **53**, 2841 (1996).
[37] B. Buck, A. C. Merchant, and S. M. Perez, Phys. Rev. Lett. **72**, 1326 (1994).
[38] F. Hoyler, P. Mohr, and G. Staudt, Phys. Rev. C **50**, 2631 (1994).
[39] F. Michel, S. Ohkubo, and G. Reidemeister, Prog. Theor. Phys. Suppl. **132**, 7 (1998).
[40] T. Sakuda and S. Ohkubo, Phys. Rev. C **57**, 1184 (1998).
[41] B. Buck, A. C. Merchant, and S. M. Perez, J. Phys. G **18**, 143 (1992).
[42] P. Mohr, Open Nucl. Part. Phys. J. **1**, 1 (2008).
[43] Database ENSDF, http://www.nndc.bnl.gov, based on Ref. [45].
[44] T. Yamaya, K. Katori, M. Fujiwara, S. Kato, and S. Ohkubo, Prog. Theor. Phys. Suppl. **132**, 73 (1998).
[45] C. M. Baglin, Nucl. Data Sheets **80**, 1 (1997).
[46] B. Buck and A. A. Pilt, Nucl. Phys. **A280**, 133 (1977).
[47] V. D. Avchukhov, K. A. Baskova, V. A. Bondarenko, A. B. Vovk, L. I. Govor, and A. D. Demidov, Izv. Akad. Nauk SSSR, Ser. Fiz. **46**, 947 (1982).
[48] J. Orce *et al.*, Phys. Rev. C **75**, 014303 (2007).
[49] F. Michel and R. Vanderpoorten, Phys. Rev. C **16**, 142 (1977).
[50] H. P. Gublar, U. Kiebele, H. O. Meyer, G. R. Plattner, and I. Sick, Nucl. Phys. **A351**, 142 (1981).
[51] L. W. Put and A. M. J. Paans, Nucl. Phys. **A291**, 93 (1977).
[52] E. Friedman, H. J. Gils, H. Rebel, and Z. Majka, Phys. Rev. Lett. **41**, 1220 (1978).
[53] H. J. Gils, E. Friedman, H. Rebel, J. Buschmann, S. Zagromski, H. Klewe-Nebenius, B. Neumann, R. Pesl, and G. Bechtold, Phys. Rev. C **21**, 1239 (1980).
[54] A. M. Kobos, B. A. Brown, R. Lindsay, and G. R. Satchler, Nucl. Phys. **A425**, 205 (1984).
[55] T. Rauscher, computer code NON-SMOKER^{WEB}, http://nucastro.org/websmoker.html.
[56] P. Demetriou and M. Axiotis, AIP Conf. Proc. **891**, 281 (2007).
[57] P. Demetriou, A. Lagoyannis, A. Spyrou, H. W. Becker, T. Konstantinopoulos, M. Axiotis, and S. Harissopulos, AIP Conf. Proc. **1090**, 293 (2009).
[58] D. T. Khoa, W. von Oertzen, and H. G. Bohlen, Phys. Rev. C **49**, 1652 (1994).
[59] L. McFadden and G. R. Satchler, Nucl. Phys. **84**, 177 (1966).
[60] K. Czerski (private communication).